Electrocatalytic Water Oxidation at Neutral pH–Deciphering the Rate Constraints for an Amorphous Cobalt-Phosphate Catalyst System

Si Liu, Ivelina Zaharieva, Luca D'Amario, Stefan Mebs, Paul Kubella, Fan Yang, Paul Beyer, Michael Haumann, and Holger Dau*

The oxygen evolution reaction (OER) is pivotal in sustainable fuel production. Neutral-pH OER reduces operational risks and enables direct coupling to electrochemical CO_2 reduction, but typically is hampered by low current densities. Here, the rate limitations in neutral-pH OER are clarified. Using cobalt-based catalyst films and phosphate ions as essential electrolyte bases, current–potential curves are recorded and simulated. Operando X-ray spectroscopy shows the potential-dependent structural changes independent of the electrolyte phosphate concentration. Operando Raman spectroscopy uncovers electrolyte acidification at a micrometer distance from the catalyst surface, limiting the Tafel slope regime to low current densities. The electrolyte proton transport is facilitated by diffusion of either phosphate ions (base pathway) or H_3O^+ ions (water pathway). The water pathway is not associated with an absolute current limit but is energetically inefficient due to the Tafel-slope increase by 60 mV dec^{-1}, shown by an uncomplicated mathematical model. The base pathway is a specific requirement in neutral-pH OER and can support high current densities, but only with accelerated buffer-base diffusion. Catalyst internal phosphate diffusion or other internal transport mechanisms do not limit the current densities. A proof-of-principle experiment shows that current densities exceeding 1 A cm^{-2} can also be achieved in neutral-pH OER.

S. Liu, I. Zaharieva, L. D'Amario, S. Mebs, P. Kubella, F. Yang, P. Beyer, M. Haumann, H. Dau
Department of Physics
Freie Universität Berlin
14167 Berlin, Germany
E-mail: holger.dau@fu-berlin.de
L. D'Amario
Department of Chemistry
Ångström Laboratory
75120 Uppsala, Sweden

1. Introduction

To limit global warming as mandated by the Paris treaty, a substantial worldwide reduction of CO_2 emission is required and approached, inter alia, through international legislation or national climate law initiatives.[1] One related task for science and engineering is the development of sustainable ways for the production of non-fossil fuels, which are energetically driven by renewable energy sources, either directly in artificial photosynthesis ("solar fuels") or indirectly using "green" electricity from the power grid (Power-to-X approach, with X being H_2 or any other energy-rich chemical).[2] Water splitting comprising water oxidation (oxygen evolution reaction, OER) and proton reduction (hydrogen evolution reaction, HER) is a promising way to achieve chemical energy storage by dihydrogen (H_2) production. For the production of carbon-based gaseous or liquid fuels (or commodity chemicals), the OER is coupled to CO_2 reduction (CO_2 reduction reaction, CO2RR). Noteworthily, the OER is a crucial step in essentially all attractive routes toward a non-fossil fuel, in analogy to the central role of the OER in biological photosynthesis.[3–5] The design of highly efficient and stable catalyst materials for OER based on non-precious, earth-abundant metals represents a key task for the development of technologies that target a sizeable contribution to global CO_2 reduction. The anodic half-reaction of water splitting and electrochemical CO_2 reduction (the OER) is considered particularly challenging, due to intrinsic energetic barriers in the OER itself and further severe kinetic limitations, the latter being investigated herein for the OER in the near-neutral pH regime.

Conventional electrochemical OER either takes place in the alkaline (pH > 13) or acidic (pH < 2) pH regime. Alkaline OER is favored by stabilization of catalytic transition metal oxyhydroxides, while at acidic pH efficient proton exchange membranes (PEM, typically Nafion membranes) can be employed.[6,7] Both alkaline and PEM water electrolysis devices are commercially available. Often a distinction between alkaline OER and acidic OER also is made when discussing reaction mechanisms.[8–12] In comparison to alkaline and acidic OER, OER in the intermediate

pH regime is less intensely investigated. Yet, OER in the near-neutral pH regime will be favorable or even essential in future technological systems, for the following reasons:
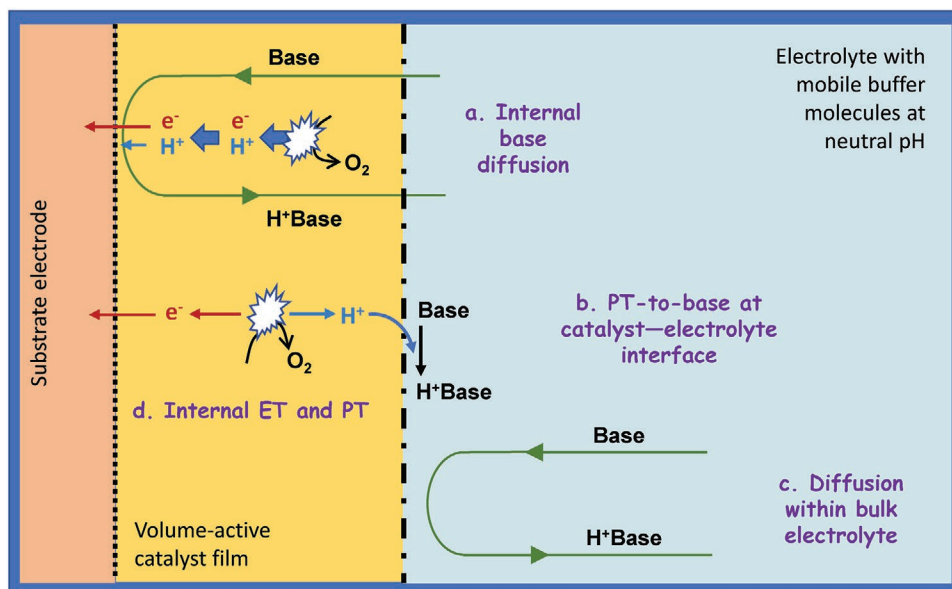
i. In comparison to OER at alkaline pH or acidic pH, neutral-pH OER often exhibits a more "benign" behavior when using complex material combinations by disfavoring degradative material transformations (corrosion), for example, in photochemical, photocatalytic, and photoelectrochemical systems.

ii. Extreme pH values and associated (health) hazards in device operation are avoided, which is a safety aspect of importance, especially in non-industrial environments such as decentralized hydrogen production by private property owners ("personalized energy").[13]

iii. Electrochemical CO_2 reduction typically requires the operation of the device at near-neutral electrolyte pH because CO_2-enriched electrolytes almost inevitably act as a bicarbonate buffer system, thereby, adjusting an operation pH close to 7.[14,15]

Amorphous, volume-active cobalt oxides (or rather oxyhydroxides), herein denoted as CoCat, with water molecules, as well as anions and cations, filling the voids between oxide fragments[16–22] currently may be the best-performing electrocatalyst material at neutral pH, as opposed to alkaline OER where inter alia $Ni_vFe_wO_x(OH)_y$ materials are superior.[23–30] Here, the amorphous CoCat material combined with a potassium phosphate (KPi) electrolyte is selected as a model system to explore the factors that limit the electrocatalytic current flow in OER at neutral pH. The CoCat material was selected because it is, structurally and functionally, especially well characterized.[17,20–22,31–44] However, we suggest that our results are generally valid for water oxidation in the near-neutral pH regime since various other material-electrolyte systems exhibit similar near-neutral OER characteristics as the CoCat-KPi system.[32,34,45,46] We note that, in line with an essential role of phosphate or alternative protonatable ions,[16] near-neutral OER in aqueous solution has been almost exclu-

sively investigated using a pH-buffer system with ions that can undergo protonation state changes in that pH regime.[14,34,47–49]

CoCat has been investigated in seminal studies by Nocera and co-workers and was denoted as a cobalt-phosphate catalyst (CoPi).[20,31,50,51] Phosphate ions are indeed an integral part of the CoCat when obtained by electrodeposition in phosphate buffer (P:Co ratio of about 1:3 in ref. [19]). There likely is a favorable structural role of phosphate ions, for example, by limiting the formation of extended defect-free catalyst domains.[22,34,35,38,52–54] Moreover, the phosphate ions have been proposed to fulfill a functional role in supporting electrocatalysis. They could be an integral constituent of the catalyst material that supports localized proton-coupled electron transfer steps[33,37,44,48] or they could act as migrating (diffusing) proton carriers.[16,21,55–57]

Although the importance of phosphate or alternative "buffer ions" is commonly accepted, we consider the experimental characterization and understanding of the technological decisive current-density–electric-potential relations (in the following denoted as "current–voltage" or "j–V" relations) as being incomplete, which motivates the present investigation. In an early study addressing the role of electrolyte bases in near-neutral-pH water oxidation, we found that for nine different protonatable ions employed as a pH-buffering system, the catalytic current density at comparably high electrode potentials (1.35 V vs NHE) does not follow a classical "thermodynamic" pH dependence.[16] It is rather determined by the electrolyte pH and the pK_a-value of the buffering groups such that the availability of a (deprotonated) proton-accepting base determines the current density.[16] To rationalize this finding, we proposed that the current-limiting process in OER is the transfer of protons from the catalyst material to unprotonated buffer molecules as it takes place at the catalyst-electrolyte interface (option b in **Scheme 1**). Costentin and co-workers modeled j–V curves for CoCat-OER and further electrokinetic data in a series of inspiring investigations.[37,40,58] In ref. [37], they suggest film-internal diffusion of the buffer molecules ($HPO_4^{2-}/H_2PO_4^-$) between the

Scheme 1. Possible rate-limiting processes in neutral-pH OER.

**ADVANCED
SCIENCE NEWS**

www.advancedsciencenews.com

**ADVANCED
ENERGY
MATERIALS**

www.advenergymat.de

external, electrolyte-exposed surface of the catalyst film and the catalyst-film–substrate-electrode interface, with phosphate ions serving as proton shuttle within the CoCat catalyst (option a in Scheme 1).[37] According to this proposal, also the CoCat-internal diffusion of phosphate ions could be a rate-determining process. Recently, we have developed an analytical model, which quantitatively explains the presence of proton transfer limitation by macroscopic diffusion of the buffer base in the bulk electrolyte, and thus, outside of the catalyst film (option c in Scheme 1).[55] This model predicts that at high catalytic potential, the maximum current density is determined by the protonation state of the buffer base, its concentration, and an effective diffusion constant describing the diffusion of the buffer ions within the bulk electrolyte. In summary, three different scenarios for the rate-limiting process in proton transport mediated by mobile phosphate ions can be distinguished (see Scheme 1): a) internal diffusion within the catalyst, b) proton transfer at the outer catalyst surface, and c) macroscopic diffusion, and thereby, proton transfer within the electrolyte. In the present study, we succeed in distinguishing between these options, thereby,

identifying the dominant rate-determining processes. Experimentally, we focus on the low current density regime because it is relevant for artificial photosynthesis applications. Furthermore, we provide a proof-of-principle experiment with high-current OER at near-neutral pH. We examine catalyst films deposited on a transparent conducting oxide, complemented by experiments with CoCat films deposited on nickel foam electrodes and a discussion of the high-current regime relevant to industrial electrolyzer systems.

2. Results and Discussion

2.1. Phosphate Dependence of *j*–*V* Curves

To investigate the role of phosphate ions in water oxidation catalyzed by CoCat at neutral pH (7), *j*–*V* curves were measured at potassium phosphate (KPi) concentrations in the electrolyte ranging from 1.6 to 250 mM, in four sets of experiments (**Figure 1**)
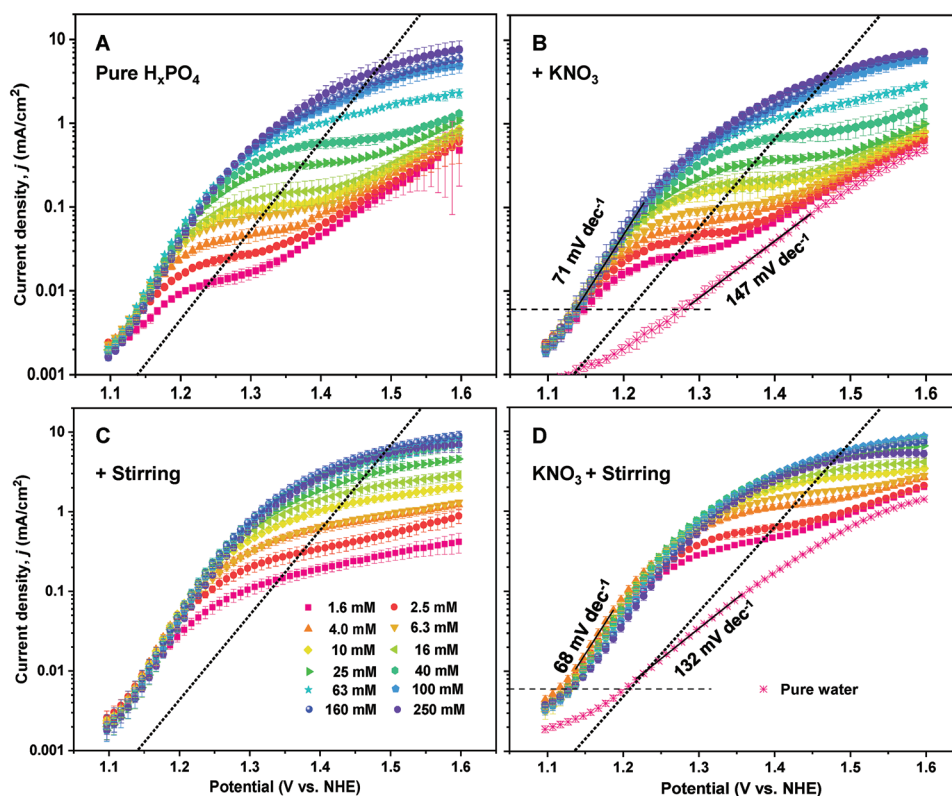

Figure 1. Phosphate concentration dependence of *j*–*V* curves investigated at pH 7. The current density (*j*) was recorded at various electrode potentials (*V* in Volt vs NHE), for the static operation of the electrochemical cell (no stirring) or with enhanced convection (stirred), without or with 500 mM KNO₃ as a supporting electrolyte component. For the collection of *j*–*V* curves, the potential was increased stepwise (from lowest to highest values) and the current density was determined after an equilibration period of 1 min at the respective potential. For each *j*–*V* curve, a fresh CoCat film had been prepared, with a deposition charge of 10 mC, corresponding to ≈100 nmol of Co ions per cm². All experiments were repeated at least three times; vertical error bars indicate standard deviations. The dotted lines mark the approximate inflection points of the *j*–*V* curves (same line in (A)–(D)), which were determined as shown in Figure S20, Supporting Information, and herein are discussed as "plateau levels." In (B) and (D), approximate Tafel slopes are indicated (rough graphical estimates, excluding the current density regime below the dashed-line level of 7 μA cm⁻² in the estimation). We note that at high phosphate concentrations, control experiments revealed a partial CoCat film loss (Figures S2–S4, Supporting Information; see also Figures S23–S25, Supporting Information, for SEM images), which explains the decrease in current density at high potentials as observed in some experiments.

A. Variation of KPi concentration without additional salts in an unstirred electrolyte solution (Figure 1A);
B. Variation of KPi concentration in high-salt (500 mm KNO_3) and unstirred electrolyte solution (Figure 1B);
C. Variation of KPi concentration without additional salts in a stirred electrolyte solution (Figure 1C);
D. Variation of KPi concentration in high-salt (500 mm KNO_3) and stirred electrolyte solution (Figure 1D).

To complement the data sets B and D, *j–V* curves were also collected in the high-salt electrolyte without any KPi and with or without stirring (initial pH adjusted to be close to 7). The same electrochemical cell configuration was used during the *j–V* curve collection to ensure identical diffusion characteristics in A and B (unstirred), as well as C and D (stirred with 500 rpm; Figure S1, Supporting Information). Analysis of Figure 1 by visual inspection and summarizing informative values in respective graphics (Figure S5, Supporting Information, and **Figure 2**) reveal.

i. Common Tafel-slope characteristics at all KPi concentrations: At low potentials (around 1.15 V vs NHE) an overlapping and approximately exponential increase of the current density (a linear increase of log *j*) is observed in all curves, suggesting similar Tafel slopes and exchange current densities (close to 70 mV dec^{-1}). Consequently, at low overpotentials, the current density is independent of the KPi buffer concentration (Figure S5, Supporting Information), as also reported in ref. [33]. Assuming that the observed Tafel slope and exchange current density reflect a specific reaction mechanism, this observation implies that the OER reaction mechanism is unaffected by the KPi concentration. Whereas the Tafel slope itself is not significantly affected by the KPi concentration, the extension of the linear regime (of log *j*) increases strongly with increasing KPi concentration, from clearly less than one decade increase in current density (for pure H_xPO_4 without stirring) to clearly more than one decade, which relates to the KPi-dependence of the plateau level in the *j–V* curves.

ii. Strongly increased Tafel slope without KPi: For the *j–V* curve collected in "pure water" (without KPi buffer, but with 500 mm KNO_3), strikingly different behavior is observed: an increase in current density with a Tafel slope that is approximately two times larger than in KPi buffer and extends over a large potential range (Figure 1B,D). This behavior is reproduced in the simulations presented further below for proton transport by H_3O^+ ions (see also in ref. [37]).

iii. Plateau level determined by KPi concentration: When increasing the applied potential beyond the Tafel slope region, a plateau level of the current density is reached at 1.25 to 1.4 V, which is well visible (in Figure 1A,B) as an inflection point of the *j–V* curves for KPi concentrations ranging from 1.6 to 40 mm. A quantitative analysis of current densities at the inflection points for various KPi concentrations is shown in Figure 2A. The plateau level is roughly proportional to the buffer concentration, in line with a current limitation determined by the availability of unprotonated buffer ions (HPO_4^{2-}) needed for accepting the "product protons" from water oxidation.[16] This current limit is clearly lower for the unstirred electrolyte
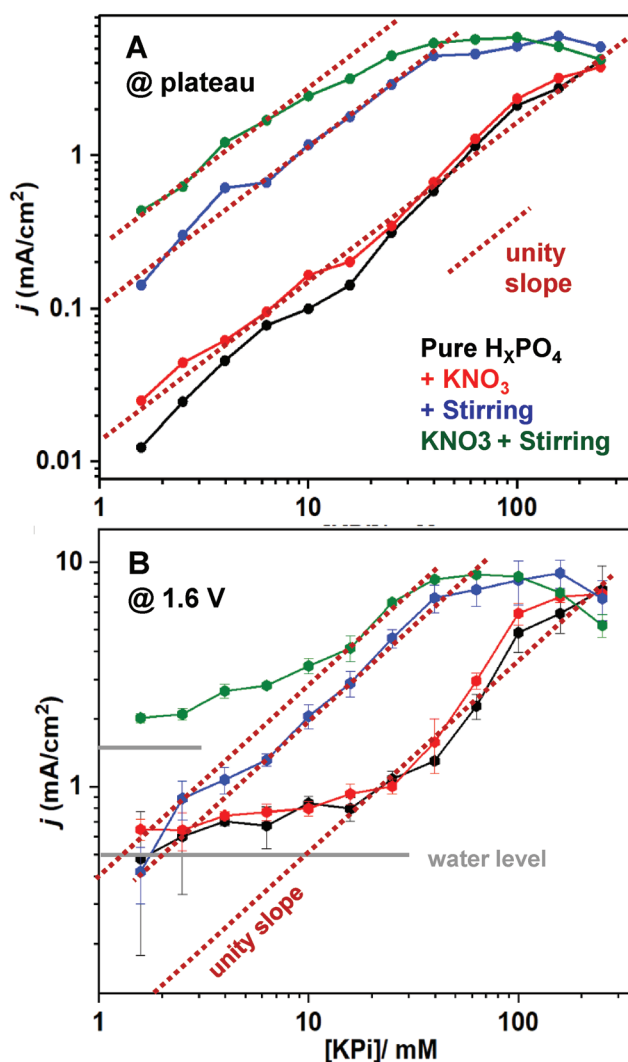
Figure 2. Current density of CoCat as a function of phosphate buffer (KPi) concentration at selected potential regions. The symbols represent the data of Figure 1, (A) in black, (B) in red, (C) in blue, and (D) in green. Panel (A) shows the characteristic current corresponding to the plateau in Figure 1. In panel (B), each point represents the current density at 1.6 V. The slope of the red dotted line is unity which corresponds to a first-order (linear) relation between current density and KPi concentration. In panel (B), the two grey lines mark current densities at 1.6 V versus NHE determined for "pure water" in the absence of KPi molecules (but with 500 mm KNO_3; see Figure 1B,D).

conditions, implying that (macroscopic) diffusion of the buffer ions is a limiting factor in catalytic turnover. The dotted unity-slope line in Figure 2A corresponds to a first-order KPi concentration dependence of the plateau level. Such a linear dependence is also found for stirred electrolytes at low current density, but at a significantly higher plateau level (about a 12-fold or 18-fold increase in low-salt or high-salt electrolytes, respectively). This finding suggests a current limitation by macroscopic KPi diffusion.

iv. Influence of ionic strength: In the experiment shown in Figure 1A, variation of the KPi concentration did not only change the availability of proton-accepting buffer molecules

**ADVANCED
SCIENCE NEWS**

www.advancedsciencenews.com

**ADVANCED
ENERGY
MATERIALS**

www.advenergymat.de

but at the same time altered the total ion concentration. To investigate whether changes in ionic strength affect the $j–V$ curves, the ionic strength was kept at a high level irrespective of the KPi concentration by adding 500 mM KNO_3 to the buffer (Figure 1B). We observe qualitatively the same $j–V$ behavior with and without KNO_3 complementation, but at very low KPi concentrations the plateau level is moderately enhanced with KNO_3 in unstirred electrolytes (by a factor of about 2, 1.8, or 1.4 at 1.6, 2.5, or 4 mM KPi). In stirred electrolytes, a comparison of the low-salt to the high-salt $j–V$ curves reveal a more pronounced high-salt enhancement than observed in the unstirred electrolyte (at low KPi concentrations), approaching a factor of three. We conclude that for a low KPi concentration also the added salt (500 mM KNO_3) plays a role in enhancing the current density. This salt effect is especially prominent at low current densities and most likely not explainable by a "normal" Ohmic resistance influence, as also confirmed by simulations discussed further below. Therefore, an ionic strength effect on either KPi diffusion or protonation states in the Helmholtz layer at the catalyst–electrolyte interface represents a more likely explanation.

v. Biphasic $j–V$ curves relating to H_2O acting as a proton acceptor: For low and intermediate KPi concentrations at high overpotentials, the $j–V$ curves approach asymptotically the $j–V$ curve obtained for operation of the catalyst film in the KNO_3-containing, but KPi-free electrolyte, as clearly visible in Figure 1B,D. Assuming that the plateau level can be explained by the exhausted proton accepting capacity of the KPi buffer close to the catalyst surface, water obviously serves as an additional proton acceptor at high overpotentials. Therefore, the current density at 1.6 V for low KPi concentrations approaches the current for the KPi-free electrolyte (Figure 2B).

vi. Ohmic limitation at high current densities: At high current densities, increasing KPi concentrations no longer results in a proportional increase of the current density (Figures 1 and 2), which largely results from Ohmic limitations. The linear current–voltage relation visible at the highest KPi concentration in Figure S6, Supporting Information, implies an Ohmic resistance close to 35 Ohm for all four data sets (dotted lines in Figure S6, Supporting Information). This Ohmic resistance is not a catalyst-intrinsic property but reflects the sum of the electrolyte resistance and the Ohmic resistance of the ITO support of the working electrode, the latter being the dominating contribution at high salt concentrations. (We note that at the highest KPi concentrations with stirred electrolyte, the current densities decrease for increasingly positive potentials exceeding about 1.5 V, which is explainable by catalyst film degradation, see Figures S2–S4, Supporting Information.)

2.2. Structure Analysis by In Situ X-Ray Absorption Spectroscopy

Phosphate and potassium ions are present in the CoCat films obtained by electrodeposition in 100 mM potassium phosphate electrolyte at a Co:K:P stoichiometry of ≈3:1:1.[19] Specifically, the phosphate ions are often assumed to be functionally relevant, that is, an integral part of the catalyst material.[20] It indeed has been shown that phosphate ions can affect the atomic structure of the catalyst significantly.[22,34,35,38,53] Because it is conceivable that structural changes result from operation in low-phosphate or phosphate-free electrolyte (via phosphate depletion), we explored this possibility by applying in situ (operando) X-ray absorption spectroscopy (XAS) at the Co K-edge for analysis of the X-ray edge region and the extended X-ray absorption fine-structure (EXAFS).

CoCat films were operated at four different KPi conditions at pH 7 with low, medium, or high phosphate buffer concentrations (1.6, 25, or 100 mM) or in the absence of any phosphate buffer; KNO_3 salt was added to maintain an approximately constant ionic strength of 0.5–0.8 M in all experiments. After equilibration at 0.75, 1.15, or 1.33 V (vs NHE, pH 7; see Supporting Information for details), EXAFS spectra were collected in situ, that is, during the operation of the electrolyte-exposed catalyst film at the respective electric potential. The electrode potentials were selected such that the complete range of accessible oxidation states of the CoCat material is covered, with the most reduced $Co^{II}Co^{III}$ state at 0.75 V, the all-Co^{III} state at 1.15 V, and a highly oxidized $Co^{III, IV}$ state at 1.33 V.[39] The resulting spectra are shown in **Figure 3** and Figure S18, Supporting Information. Edge spectra and complete EXAFS spectra were recorded at room temperature within only 5 min at a low-flux bending-magnet beamline (≈10^{10} photons per s at the Co K-edge) with an extended irradiated sample area (about 5 mm^2). Under these experimental conditions, the X-ray dose per area is especially low, which prevents sample modifications caused by X-ray irradiation (radiation damage), as also verified in ref. [59] for CoCat electrode films. Further details are provided in the Supporting Information.

Analysis of the X-ray edge spectra resulted in estimates of the Co oxidation states (**Table 1**), which ranged from the mixed-valent $Co^{II}_{0.4}Co^{III}_{0.6}$ state (at 0.75 V) via the all-Co^{III} state (at 1.15 V) to the mixed valent $Co^{III}_{0.85}Co^{IV}_{0.15}$ state (at 1.33 V), in good agreement with previous results.[39,43] These oxidation state estimates are, within the limits of accuracy, independent of the KPi concentration.

In the Fourier-transformed EXAFS spectra, the two main peaks correspond to the oxygen ligands in the first Co coordination sphere (Co−O bonds of ≈1.9 Å), and the Co ions in the second coordination sphere of the X-ray absorbing Co atom (Co−Co distance of ≈2.8 Å), respectively. The amplitudes of these two peaks correspond to the abundance of the respective Co−O and Co−Co motifs in the material.

Based on the analysis of the EXAFS data in Figure 3 we conclude

i. Taking the noise level into account and comparing the amplitudes of Co−O and Co−Co interactions at different phosphate concentrations, the difference between spectra collected at the same potential is negligible. There are no indications for structural changes in the CoCat film that relate to operation at different phosphate concentrations.

ii. The potential dependence of the peak amplitudes is highlighted by horizontal bars in Figure 3 and is fully consistent with our previous results.[39]

The above conclusions were drawn from a visual inspection of EXAFS spectra in Figure 3 and are fully confirmed by EXAFS simulations (Tables S5 and S8, Supporting Information). The
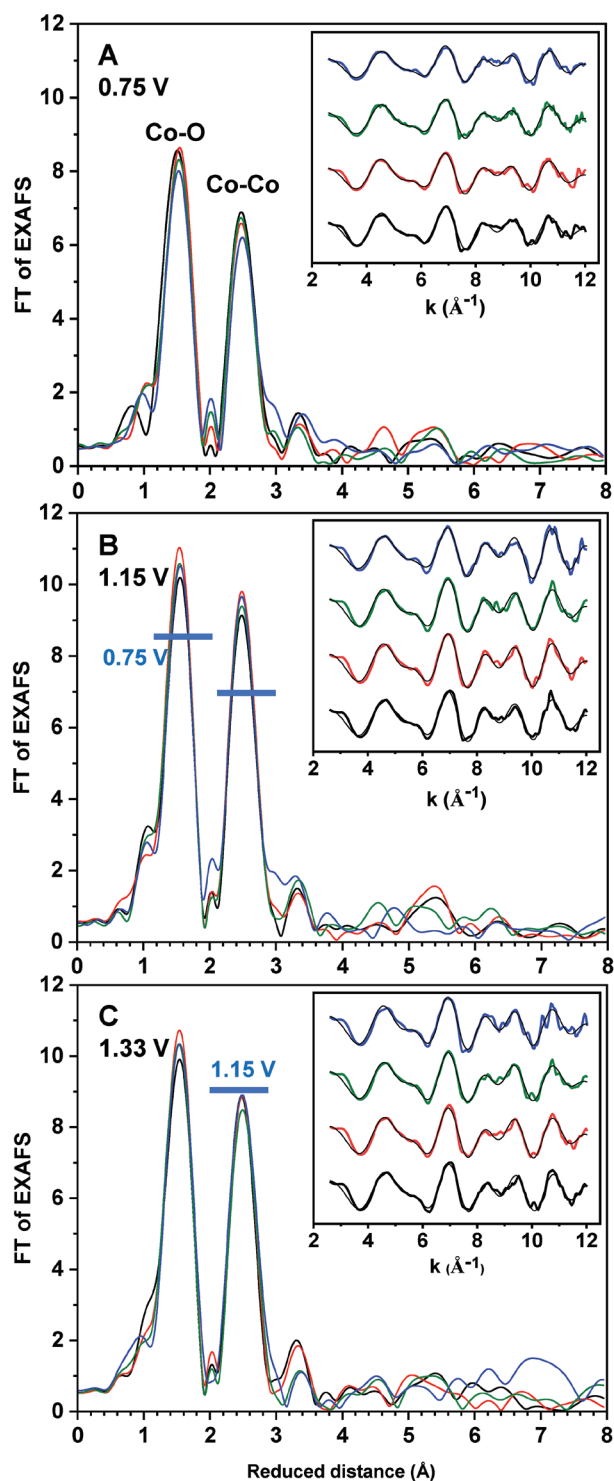
Figure 3. In situ EXAFS spectra at the Co K-edge at different phosphate buffer concentrations during electrochemical operation at A) 0.75 V, B) 1.15 V, or C) 1.33 V (potentials vs NHE, pH 7). Fourier-transforms (FTs) of experimental k^3-weighted EXAFS spectra are shown for phosphate buffer (KPi) concentrations of zero (blue), 1.6 mM (green), 25 mM (red), or 100 mM (black). The insets show the k^3-weighted EXAFS data on a wavevector scale (colored lines), as well as the respective least-square simulations (thin black lines). Further details on the EXAFS experiment and data analysis are provided in Supporting Information.

EXAFS simulations reveal that at all phosphate concentrations, the transition from the $Co_{0.6}^{II}Co_{0.4}^{III}$ state (at 0.75 V) to the all-Co^{III} state (at 1.15 V) is associated with i) a shortening of the mean Co—O bond lengths from 1.90 to 1.87 Å, as expected for an oxidation state increase, ii) a rise of the first-sphere mean Co-coordination number from 5 to 6, and iii) increased di-μ-oxo bridging between Co ions. The transition from the all-Co^{III} state to the $Co_{0.85}^{III}Co_{0.15}^{IV}$ state is associated with a further shortening of Co—O bond lengths, in line with Co^{IV} formation, and subtle differences in either the amount or distance spread of the 2.82 Å EXAFS interactions. A more detailed discussion of the potential-dependent structural changes and their likely mechanistic relevance has been provided elsewhere, based on XAS results for CoCat operation in 100 mM phosphate electrolyte.[39,43] Now the same potential-dependent changes in atomic structure are detected at all investigated electrolyte phosphate concentrations. Regarding the mechanistic role of phosphate ions, we conclude that the redox dynamics of the CoCat material are independent of the electrolyte phosphate concentration during CoCat operation.

2.3. Internal Phosphate Amount

Bediako et al. suggested proton transport by phosphate ions that diffuse within the catalyst material.[37] If this process were related directly to the first-order KPi dependence of the plateau-level current density in the j–V curves of Figure 1, then the electrolyte phosphate concentration should correlate with the internal phosphate amount. Therefore, we explored the correlation between catalyst-internal phosphate amount and electrolyte phosphate concentration for catalyst operation in the sub-catalytic (1 V) and catalytic (1.3 V) regimes. After operation at the respective potential, the catalyst film was quickly removed from the electrolyte and rinsed with Milli-Q water, followed by the analysis of the phosphate content, as detailed in the Supporting Information. We note that water rinsing or immersion in reagent water represents a reproducible procedure to remove excess electrolyte ions,[61,62] as we confirmed by comparative SEM analyses (Figure S21, Supporting Information). In conclusion, the results of **Figure 4** not only argue against the effective exchange of phosphate ions between electrolyte and catalyst material but also rule out the possibility that the first-order phosphate concentration dependence of current density can be explained by correspondingly increased catalyst-internal phosphate concentrations.

2.4. Local pH Monitored by In Situ Raman Spectroscopy

We propose the following scenario: The plateau-level current density of the j–V curves of Figure 1 is controlled by the availability of a buffer base (HPO_4^{2-}) close to the CoCat electrode. In the Tafel slope regime, this base mitigates local electrolyte acidification by accepting the protons produced by the OER. The plateau-level of the current density is reached once diffusion of the buffer ions between CoCat anode and cathode (here a Pt counter electrode) approaches its maximally possible rate, resulting in pronounced local acidification of the electrolyte close to the electrolyte-catalyst interface.

**ADVANCED
SCIENCE NEWS**

www.advancedsciencenews.com

**ADVANCED
ENERGY
MATERIALS**

www.advenergymat.de

Table 1. Cobalt K-edge positions and oxidation states (Ox. state) of CoCat films (20 mC cm^{-2}) operated at various KPi concentrations and electrode potentials.

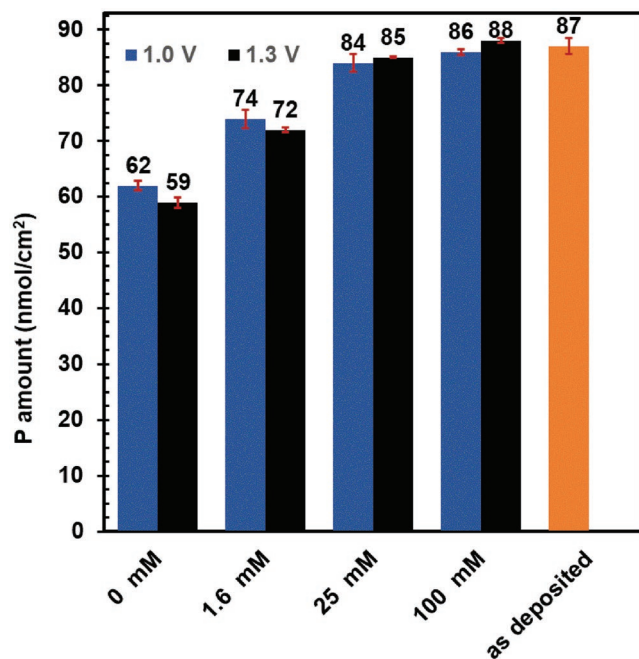| KPi concentration [mM]	0.75 V_{NHE}		1.15 V_{NHE}		1.33 V_{NHE}	
	Edge position [eV]	Ox. state	Edge position [eV]	Ox. state	Edge position [eV]	Ox. state
0	7719.92	2.60	7720.78	2.97	7721.12	3.12
1.6	7719.91	2.60	7720.80	2.98	7721.11	3.12
25	7719.91	2.60	7720.85	3.00	7721.16	3.14
100	7719.93	2.61	7720.77	2.97	7721.18	3.15

Edge position spectra were determined from the edge spectra by the integral method.[60] The experimental error of the edge positions is around 0.1 eV; the oxidation states were estimated based on a calibration curve obtained for simple cobalt oxides (see ref. [39]).

To verify the above scenario, we investigated the local pH close to the outer catalyst–electrolyte interface using Raman spectroscopy.

Direct or indirect pH measurements in electrochemical systems via electrochemical or optical methods have been previously reported, including the use of pH-sensitive electrodes, rotating disk electrodes (RDE), fluorescence microscopy, and Raman or infrared spectroscopy.[63–69] Here, in situ Raman spectroscopy was employed to study during electrocatalysis the near-electrode pH at about 20 µm distance to the outer CoCat surface (**Figure 5**), using the basic rationale described earlier for estimation of the local pH values during CO_2 reduction[70] (see also ref. [67]). The advantage of the Raman approach is good spatial resolution (0.5–5 µm) and its largely non-invasive character (some influence of heating of the catalyst film by absorbed laser light cannot be excluded). The pH determination rationale is based on amplitude changes of vibrational

bands assignable to changes in the protonation state of phosphate species, as detailed in the Supporting Information. In Figure 5A, the intermediate band at 991 cm^{-1} corresponding to the basic phosphate species (HPO_4^{2-}) sharply decreases when applying increasingly positive potentials, whereas the bands at 877 and 1077 cm^{-1} corresponding to the protonated base (i.e., $H_2PO_4^-$) rise. The quantitative analysis takes into account broad potential-dependent bands from the CoCat material[71] as shown in Figure 5B and results in the potential dependence of the local pH close to the outer CoCat surface, which is shown in Figure 5C.

We observe pronounced local acidification by almost one pH unit close to the outer CoCat surface for electric potentials beyond the Tafel-slope regime. This finding supports that, during OER operation, macroscopic proton transport limitations result in a local pH decrease (increased proton activity) in the vicinity of the catalyst surface, which in turn limits the catalytic current density. We emphasize that of the four options of rate-limiting processes in neutral-pH OER, which are indicated in Scheme 1, only the macroscopic proton transport limitation is predicted to result in pronounced local acidification in the electrolyte phase near the outer catalyst surface. The verification of electrolyte acidification close to the outer catalyst surface forms the cornerstone for the quantitative modeling of j–V curves described in the following.

2.5. Simulation of j–V Curves

The four sets of j–V curves in Figure 1 were simulated by a model, which describes the influence of proton transport within the electrolyte on the potential dependence of the current density and is schematically shown in **Scheme 2**. For further details of the underlying analytical model and its computational implementation, see ref. [55] and Supporting Information.

In **Figure 6**, simulation results are compared to experimental j–V curves for three simulation approaches:

1st) The simulations shown in panels A to D involve a minimal set of variable parameters. For each set of j–V curves, the 12 j–V curves obtained for 12 phosphate concentrations were simulated with identical values for I_0, k_{dPi}, and k_{dH+}. Only the Tafel slopes were adapted individually for each curve by least-square curve-fitting, resulting in only minimal variations (within 1% of 76 mV dec^{-1}). For current densities below about 200 µA cm^{-2}, the experimental and simulated curves agree reasonably well. Therefore, we conclude that in the low
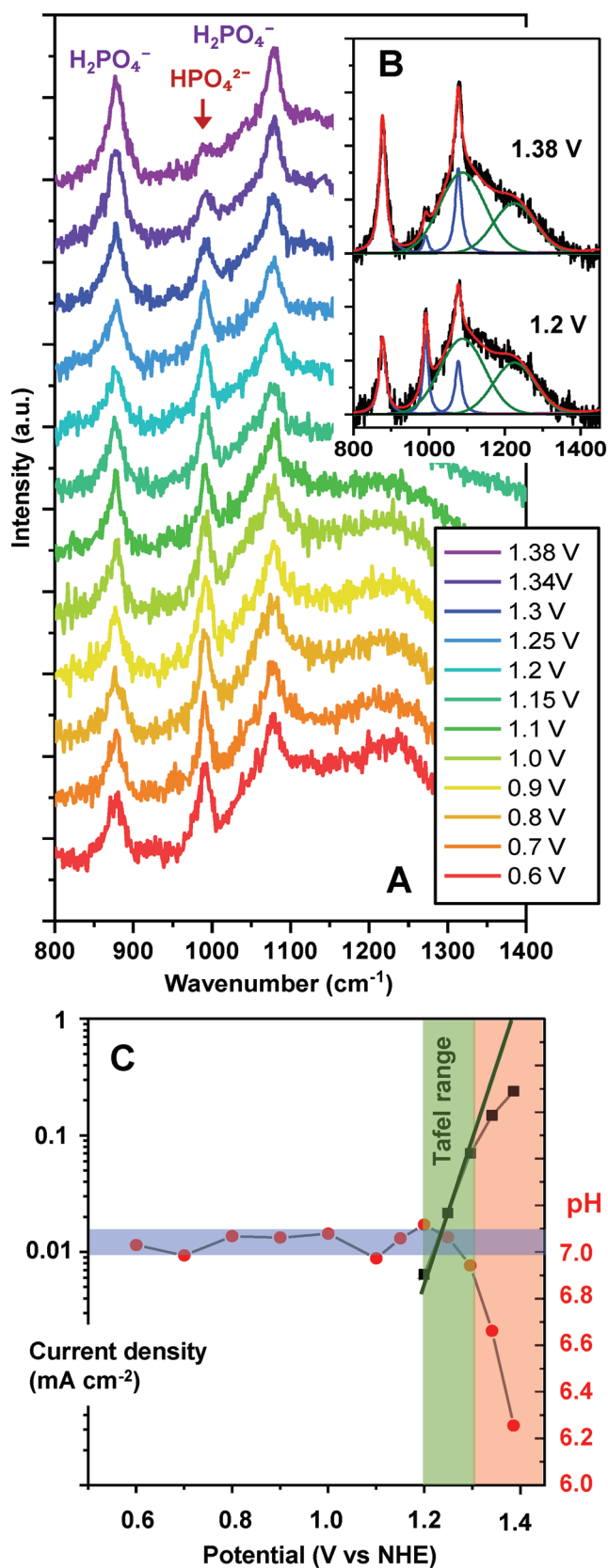

Figure 4. Quantification of phosphate amounts within CoCat films at selected KPi concentrations and electrode potentials. The blue and black bars show values from films operated at 1 and 1.3 V versus NHE, respectively. The phosphate amount in the as-deposited film (deposited in 100 mM KPi) without further electrochemical operation is shown as an orange bar.

**ADVANCED
SCIENCE NEWS**

www.advancedsciencenews.com

**ADVANCED
ENERGY
MATERIALS**

www.advenergymat.de

current regime, the rate-limiting effect of the buffer and the water pathway of electrolyte proton transport are well predicted by the model of Scheme 2. At higher current densities, however, a further rate-limitation comes into play, which is the Ohmic resistance (see Section 2.1-*vi*).

2nd) The 2nd simulation approach differs from the 1st one by the introduction of an Ohmic resistance term, where the resistance value (*R*) was adapted for each *j–V* curve individually. Excellent agreement is obtained for most *j–V* curves (panels E–H in Figure 6). At high current densities (reached at high KPi concentrations), however, the experimental current densities exceeded the simulated curves significantly (see Figures 6E and 6F), revealing an "enhancement" effect in the experimental *j–V* curves.
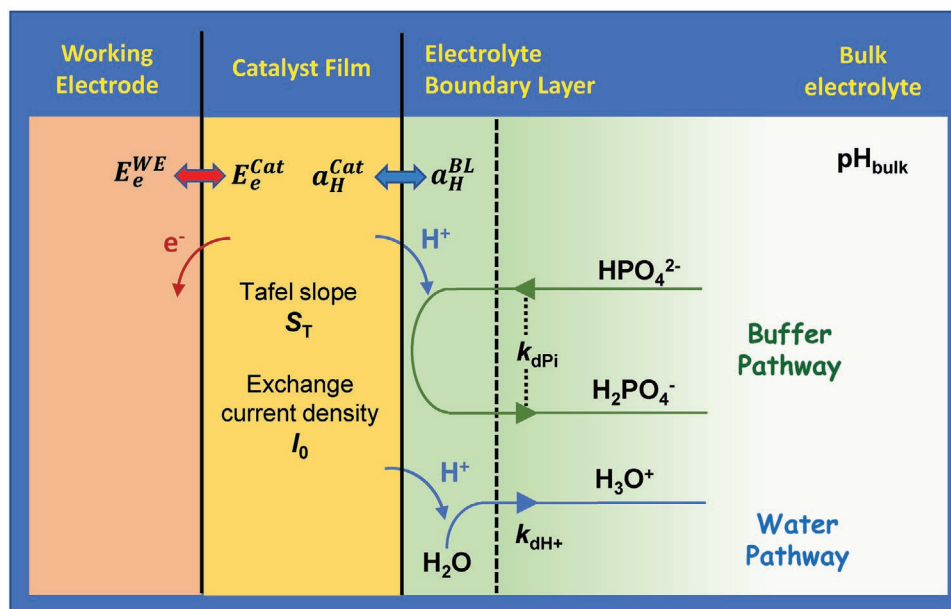
3rd) We assign the above enhancement effect to accelerated diffusion at high current density resulting from bubble formation and buoyancy effects.[72] To provide an approximate description of the enhanced diffusion at high current density, the 3rd simulation approach involved a variation of k_{dPi} for individual *j–V* curves. Here, parameter correlations hamper the determination of *R* and k_{dPi} values severely, especially in the experiments with stirred solutions. We conclude that accelerated diffusion at high current densities is in line with the experimental *j–V* data. Although plausible, further investigations are required to confirm the here suggested accelerated diffusion.

The modeling approaches used elsewhere[37,40,58] were significantly more complex because they also included various catalyst film-internal processes that potentially could limit current densities. The success of the comparably simple model we used herein suggests that aside from the pivotal electrolyte proton transport by buffer ions and water molecules (plus expected Ohmic resistance effects), there is no need to expand the modeling approach in order to describe the herein investigated *j–V* curves. The simulations do not provide any indications that the potentially rate-limiting processes a, b, and d in Scheme 1 are relevant limiting factors in the here investigated *j–V* curves of CoCat water oxidation at neutral pH. However, we cannot rule out the possibility that with significantly thicker catalyst films, additional limitations in terms of the internal transport of electrons and protons might also come into play.

In the experiment of Figure 1 at high potential (e.g., 1.6 V vs NHE), the current densities attributed to the base pathway (phosphate buffer present at high concentration) and water pathway (without phosphate buffer) differ by roughly one order

Figure 5. Estimation of local acidification by in situ Raman experiments for electrocatalytic operation in 25 mM KPi buffer at pH 7 (CoCat deposition amount of 20 mC cm^{-2}). A) Spectra collected for CoCat films operated at the indicated electrode potentials (in V vs NHE); from bottom to top, the applied potential was increased stepwise. B) Examples of simulations for Raman spectra collected at 1.2 or 1.38 V versus NHE. The spectra were background subtracted and simulated from 800 to 1400 cm^{-1} as described in Supporting Information. Briefly, for each spectrum, three Lorentzian functions (blue lines) and two Gaussian functions (green lines) were fitted with fixed band positions (Lorentzian: 877, 991, and 1077 cm^{-1}; Gaussian: 1088 and 1225 cm^{-1}) and widths (half-width at half-maximum: Lorentzian: 25, 8, and 10 cm^{-1}; Gaussian: 70 and 65 cm^{-1}), but varying band amplitudes. C) Catalytic current densities (left *y*-axis, brown squares) and local pH (right *y*-axis, red circles) determined by in situ Raman. The squares indicate static current densities after applying the respective potential for 2.5 min (current densities below 7 µA cm^{-2} are not shown).

**ADVANCED
SCIENCE NEWS**

www.advancedsciencenews.com

**ADVANCED
ENERGY
MATERIALS**

www.advenergymat.de

Scheme 2. Modeling j–V curves by considering rate-limiting electrolyte proton transport via both the buffer-base pathway and the water pathway. It is assumed that in the interior of the catalyst film, electron and proton transfer is fast (not rate-limiting); consequently, electric potential and proton activity do not vary within the catalyst material. Moreover, rapid equilibration of the proton activity between the boundary layer (a_H^{cat}) and the catalyst interior (a_H^{BL}) is assumed so that $a_H^{cat} = a_H^{BL}$. The protons produced during OER are accepted either by a buffer base molecule (HPO_4^-) or a water molecule, where the proton transfer between the catalyst film and the accepting molecule is not a rate-limiting factor. The parameters S_T and I_0 represent the Tafel slope and exchange current density, which describes the catalytic properties of the catalyst material. The diffusion of HPO_4^{2-} and $H_2PO_4^-$ are described by the diffusion constant k_{dPi}; proton diffusion is described by k_{dH+}. These are effective diffusion constants with values that depend on the geometry of the electrochemical cell, as well as diffusion accelerating factors (mechanical stirring, possibly further convective flows). All simulations were performed for the experimental pH value ($pH_{bulk} = 7$).

of magnitude (15 times in Figure 1B and 6 times in Figure 1D), whereas several orders of magnitude larger base pathway current would be expected based on the observed difference in Tafel slope. The simulations confirm an explanation that roots in the distinctly different character of the proton transport limitations, which in the case of the base pathway results in a saturation-type behavior of the j–V curves, with an absolute maximal current density (Equation (S6), Supporting Information), relating to depletion of the unprotonated phosphate base at the anode. In the case of the water pathway, a similar saturation behavior is neither observed nor predicted. Instead, the proton transport limitation results in a strongly increased Tafel slope for the water pathway. See Equations (S7)–(S11), Supporting Information, which predicts an increase of the catalyst-intrinsic Tafel slope by about 60 mV dec^{-1}. The Tafel-slope increase applies to near-neutral OER for sizeable currents supported by the water pathway of electrolyte proton transport and low (or no) current supported by the base pathway. Consequently, the water pathway can outcompete the base pathway at high potentials, but at the price of high energetic losses due to exceedingly high overpotential requirements.

Is there any relevant synergistic effect between the base pathway and water pathway of electrolyte proton transport or are the respective current density merely additive? Visual comparison of the j–V curves in Figure 1B,D obtained for electrolytes without phosphate and in the presence of low phosphate concentrations suggests that the current densities supported by each pathway roughly add up to the total current density. Similarly, also the simulations of j–V curves, which are based

on a model of additive contributions, do not provide clear indications for a mismatch between simulated and experimental curves that would require an extension of the model by synergistic effects.

2.6. High Current Densities are Achievable

The current densities in the neutral-pH j–V curves for the amorphous Cobalt phosphate system with ITO as substrate electrode never exceed 10 mA cm^{-2}. As shown above, current limitations result from both limited availability of proton-transporting buffer bases, as well as the Ohmic resistance of the electrolyte, and in particular, of the ITO substrate electrode. To reach higher current densities, we replaced the ITO substrate with a Ni foam of negligible Ohmic resistance and increased the amount of deposited CoCat material by a factor of 30 on the metallic foam with roughly 30-fold increased electrochemical surface area (when compared to a planar substrate electrode). Thereby, current densities beyond 10 mA cm^{-2} were reached (Figures S10 and S11, Supporting Information). The experimental j–V curves of the CoCat film deposited on Ni foam were simulated using identical k_{dpi} values as they were employed for simulations (using the 3rd simulation approach) of the respective data sets of Figure 1, which resulted in reasonably good simulations (Figure S11, Supporting Information). This finding shows that neither the increased surface area of the Ni foam nor the increased amount of catalytically active catalyst material modifies the current limitations assignable to macroscopic
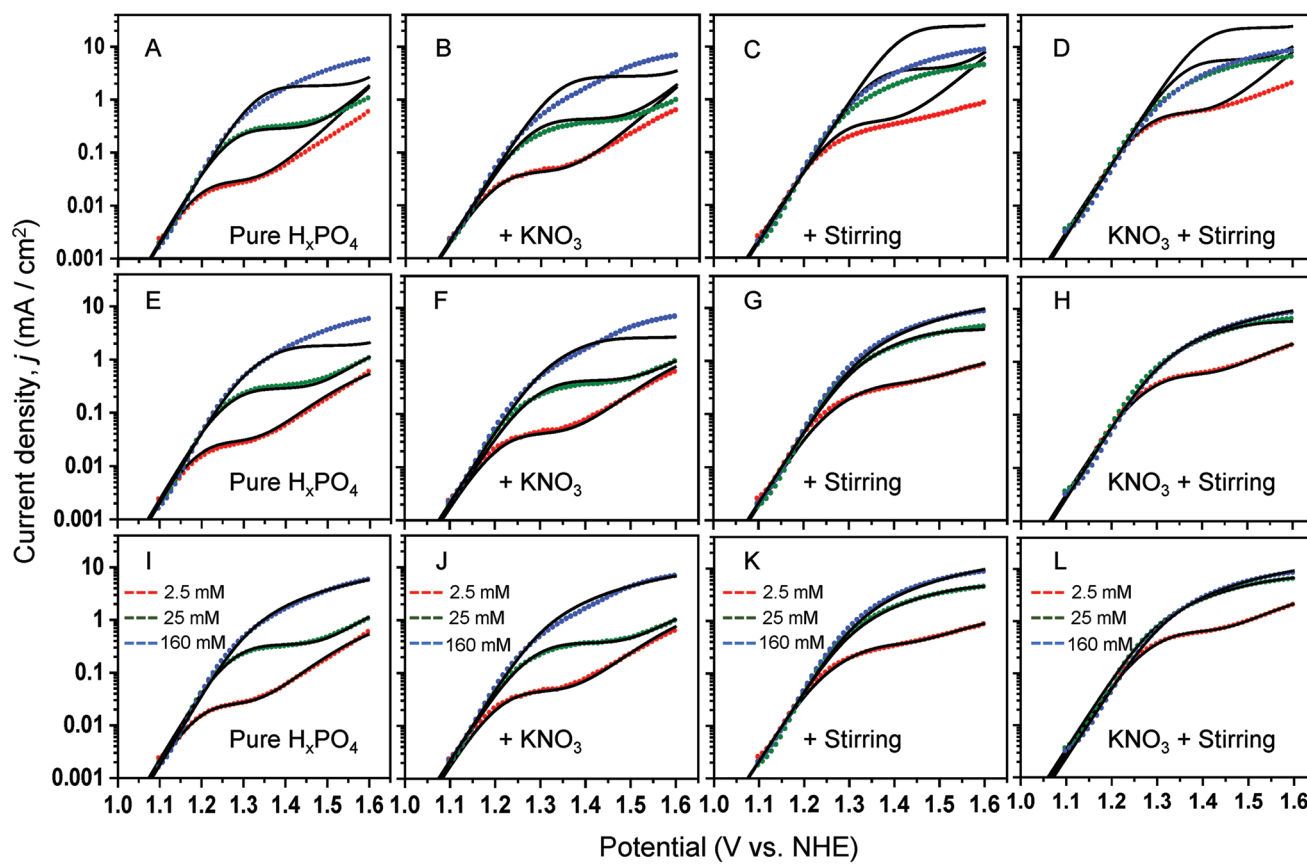
Figure 6. Experimental and simulated current densities versus the electric potential for the four sets of experimental *j*–*V* curves in Figure 1. We selected for presentation *j*–*V* curves for low (2.5 mM), intermediate (25 mM), and high (160 mM) potassium phosphate concentration; the complete sets of simulated curves are shown in Figures S7–S9, Supporting Information (simulation parameters listed in Tables S1–S3, Supporting Information). The experimental data is indicated by colored points, the simulated curves are shown as black lines. The left column of panels (A), (E), (I) relates to the experimental data of Figure 1A (pure H$_x$PO$_4$); the column with panels (B), (F), and (J) relates to Figure 1B (+ KNO$_3$); (C), (G), and (K) relate to Figure 1C (+ Stirring); (D), (H), and (L) relate to Figure 1D (+ KNO$_3$ + Stirring). The first, second, and third rows of panels relate to the 1st, 2nd, and 3rd simulation approaches described in the main text.

proton transport by buffer molecules. We observe the same current-limiting mechanisms as identified in the current regime below 10 mA cm^{-2}.

In a proof-of-principle experiment, we realized a three-electrode rapid-flow system and achieved OER current densities well above 1 A cm^{-1}. A current density of about 500 mA cm^{-2} was reached at 1.4 V (vs NHE, pH 7 of the flowing electrolyte with 1 M KPi), about 250 times greater than the maximal current in the data sets of Figure 1B. For details, see Figure S17, Supporting Information, and its figure caption; a similar "recipe" had been applied in ref. [31]. We note that despite high current densities at five times the catalyst layer thickness (when compared to the catalyst films of Figure 1 and Figure S17, Supporting Information), there is no obvious evidence of incipient catalyst-internal charge transport limitation. In summary, we present a proof-of-principle experiment that does not represent a technical electrolyzer system due to the use of a three-electrode cell with optimized reference electrode positioning. Nonetheless, this experiment demonstrates that by consistently removing the limitations identified here, technically relevant current densities at reasonable overpotential are achievable also in neutral-pH OER.

3. Conclusions

The rate-limiting factors in electrochemical neutral-pH water oxidation (OER) were investigated for volume-active CoCat films, aiming at basic understanding and generic insights not specifically related to the CoCat material. Electrokinetic and in situ XAS data show that the intrinsic mechanism of the CoCat-internal OER catalysis is unaffected by the external electrolyte phosphate concentration. On this basis, we conclude

A. Decisive limitation by macroscopic electrolyte proton transport: In situ Raman spectroscopy reveals that OER beyond the Tafel-slope regime is associated with electrolyte acidification at the catalyst electrode. Consequently, equilibration of catalyst-internal and catalyst-external (electrolyte) proton activities diminishes the pH-sensitive OER catalysis, and thereby, limits the Tafel-slope range. The observed acidification results from limited buffer diffusion between the anode and cathode causing Base$^-$ (HPO$_4^{2-}$) depletion and HBase (H$_2$PO$_4^{1-}$) accumulation at the anode. The in situ Raman experiment is conclusive because slow charge carrier transport within the catalyst or from the catalyst material to an electrolyte acceptor

base is not predicted to decrease the near-electrode electrolyte pH. Of the four options in Scheme 1, only the macroscopic electrolyte proton transport, by the $H_2PO_4^{2-}/HPO_4^-$ shuttle, is identified as a decisive rate-limiting factor.

B. Two modes of electrolyte proton transport–inefficient water and efficient base pathway: Two pathways for proton transport between anode and cathode are identified: i) the $H_2PO_4^{2-}/HPO_4^-$ shuttle and ii) the water pathway with proton-loading of H_2O molecules followed by H_3O^+ diffusion (see Scheme 2). The water pathway is technologically irrelevant in OER at neutral pH because it requires especially high overpotentials, which results in a strongly increased Tafel slope for water as a proton acceptor, as found experimentally, reproduced in simulations, and straightforwardly derived from an uncomplicated mathematical model. The base pathway is essential for efficient water oxidation at neutral pH or in the near-neutral pH regime.

C. Guidelines for technical electrolysis at neutral pH: At neutral pH, high-current operation in the Tafel-slope regime is feasible if not only Ohmic resistance effects but also catalyst-external proton transport limitations are minimized. Aside from a technically irrelevant synergism observed at very low ionic strength, increased electrical conductivity does not enhance electrolyte proton transport. Limiting base-diffusion rates cannot be overcome by an overpotential increase, in contrast to Ohmic limitations, and thus represent an especially severe, absolute current limit for the respective electrolyzer system. The above limitations already can come into play in the current range of 5–20 mA cm^{-1}, which is a current regime of relevance for the direct combination of OER catalysis with light-active materials in artificial photosynthesis devices. Yet, a proof-of-principle experiment shows that current densities exceeding 1 A cm^{-2} can be reached also in neutral pH OER for:

– high loading of the volume-active catalyst material,
– avoidance of Ohmic limitations,
– and accelerated diffusion of proton-transporting buffer molecules.

Only the latter point is a specific requirement for high-current electrocatalysis at neutral pH, resulting from the inefficiency of proton transport via the water pathway in the neutral pH regime. Catalyst-specific performance characteristics (Tafel slopes, exchange current densities) remain relevant overpotential determinants also in neutral-pH OER, but only as long as the current regime of limiting proton transport capacity is not reached.

Supporting Information

Supporting Information is available from the Wiley Online Library or from the author.

Acknowledgements

Conflict of Interest

The authors declare no conflict of interest.

Data Availability Statement

The data that support the findings of this study are available in the supplementary material of this article.

[1] European Union, Long-term low greenhouse gas emission development strategies (LT-LEDS), https://ec.europa.eu/clima/eu-action/climate-strategies-targets/2050-long-term-strategy_en, (accessed: March 2020).
[2] H. Dau, E. Fujita, L. Sun, *ChemSusChem* **2017**, *10*, 4228.
[3] N. S. Lewis, D. G. Nocera, *Proc. Natl. Acad. Sci. U. S. A.* **2006**, *103*, 15729.
[4] S. Chu, A. Majumdar, *Nature* **2012**, *488*, 294.
[5] H. Dau, C. Limberg, T. Reier, M. Risch, S. Roggan, P. Strasser, *ChemCatChem* **2010**, *2*, 724.
[6] M. Plevová, J. Hnát, K. Bouzek, *J. Power Sources* **2021**, *507*, 230072.
[7] M. Carmo, D. L. Fritz, J. Mergel, D. Stolten, *Int. J. Hydrogen Energy* **2013**, *38*, 4901.
[8] H.-Y. Qu, X. He, Y. Wang, S. Hou, *Appl. Sci.* **2021**, *11*, 4320.
[9] E. Fabbri, T. J. Schmidt, *ACS Catal.* **2018**, *8*, 9765.
[10] Z. Shi, X. Wang, J. Ge, C. Liu, W. Xing, *Nanoscale* **2020**, *12*, 13249.
[11] Q. Liang, G. Brocks, A. Bieberle-Hütter, *J. Phys. Energy* **2021**, *3*, 026001.
[12] T. Reier, H. N. Nong, D. Teschner, R. Schlögl, P. Strasser, *Adv. Energy Mater.* **2017**, *7*, 1601275.
[13] D. G. Nocera, *Inorg. Chem.* **2009**, *48*, 10001.
[14] J. Villalobos, D. González-Flores, R. Urcuyo, M. L. Montero, G. Schuck, P. Beyer, M. Risch, *Adv. Energy Mater.* **2021**, *11*, 2101737.
[15] L. Q. Zhou, C. Ling, H. Zhou, X. Wang, J. Liao, G. K. Reddy, L. Deng, T. C. Peck, R. Zhang, M. S. Whittingham, C. Wang, C.-W. Chu, Y. Yao, H. Jia, *Nat. Commun.* **2019**, *10*, 4081.
[16] K. Klingan, F. Ringleb, I. Zaharieva, J. Heidkamp, P. Chernev, D. Gonzalez-Flores, M. Risch, A. Fischer, H. Dau, *ChemSusChem* **2014**, *7*, 1301.
[17] M. Risch, V. Khare, I. Zaharieva, L. Gerencser, P. Chernev, H. Dau, *J. Am. Chem. Soc.* **2009**, *131*, 6936.
[18] G. Mattioli, P. Giannozzi, A. Amore Bonapasta, L. Guidoni, *J. Am. Chem. Soc.* **2013**, *135*, 15353.

[19] M. W. Kanan, D. G. Nocera, *Science* **2008**, *321*, 1072.

[20] D. A. Lutterman, Y. Surendranath, D. G. Nocera, *J. Am. Chem. Soc.* **2009**, *131*, 3838.

[21] M. W. Kanan, J. Yano, Y. Surendranath, M. Dinca, V. K. Yachandra, D. G. Nocera, *J. Am. Chem. Soc.* **2010**, *132*, 13692.

[22] P. W. Du, O. Kokhan, K. W. Chapman, P. J. Chupas, D. M. Tiede, *J. Am. Chem. Soc.* **2012**, *134*, 11096.

[23] M. Gorlin, P. Chernev, J. F. De Araujo, T. Reier, S. Dresp, B. Paul, R. Krahnert, H. Dau, P. Strasser, *J. Am. Chem. Soc.* **2016**, *138*, 5603.

[24] M. Gorlin, J. F. De Araujo, H. Schmies, D. Bernsmeier, S. Dresp, M. Gliech, Z. Jusys, P. Chernev, R. Kraehnert, H. Dau, P. Strasser, *J. Am. Chem. Soc.* **2017**, *139*, 2070.

[25] D. Friebel, M. W. Louie, M. Bajdich, K. E. Sanwald, Y. Cai, A. M. Wise, M. J. Cheng, D. Sokaras, T. C. Weng, R. Alonso-Mori, R. C. Davis, J. R. Bargar, J. K. Norskov, A. Nilsson, A. T. Bell, *J. Am. Chem. Soc.* **2015**, *137*, 1305.

[26] C. Roy, B. Sebok, S. B. Scott, E. M. Fiordaliso, J. E. Sørensen, A. Bodin, D. B. Trimarco, C. D. Damsgaard, P. C. K. Vesborg, O. Hansen, I. E. L. Stephens, J. Kibsgaard, I. Chorkendorff, *Nat. Catal.* **2018**, *1*, 820.

[27] M. Gorlin, P. Chernev, P. Paciok, C. W. Tai, J. Ferreira De Araujo, T. Reier, M. Heggen, R. Dunin-Borkowski, P. Strasser, H. Dau, *Chem. Commun.* **2019**, *55*, 818.

[28] D. González-Flores, K. Klingan, P. Chernev, S. Loos, M. R. Mohammadi, C. Pasquini, P. Kubella, I. Zaharieva, R. D. L. Smith, H. Dau, *Sustainable Energy Fuels* **2018**, *2*, 1986.

[29] F. Dionigi, Z. Zeng, I. Sinev, T. Merzdorf, S. Deshpande, M. B. Lopez, S. Kunze, I. Zegkinoglou, H. Sarodnik, D. Fan, A. Bergmann, J. Drnec, J. F. D. Araujo, M. Gliech, D. Teschner, J. Zhu, W.-X. Li, J. Greeley, B. R. Cuenya, P. Strasser, *Nat. Commun.* **2020**, *11*, 2522.

[30] F. Dionigi, P. Strasser, *Adv. Energy Mater.* **2016**, *6*, 1600621.

[31] A. J. Esswein, Y. Surendranath, S. Y. Reece, D. G. Nocera, *Energy Environ. Sci.* **2011**, *4*, 499.

[32] J. B. Gerken, J. G. Mcalpin, J. Y. C. Chen, M. L. Rigsby, W. H. Casey, R. D. Britt, S. S. Stahl, *J. Am. Chem. Soc.* **2011**, *133*, 14431.

[33] Y. Surendranath, M. W. Kanan, D. G. Nocera, *J. Am. Chem. Soc.* **2010**, *132*, 16501.

[34] M. Risch, K. Klingan, F. Ringleb, P. Chernev, I. Zaharieva, A. Fischer, H. Dau, *ChemSusChem* **2012**, *5*, 542.

[35] S. J. Harley, H. E. Mason, J. G. Mcalpin, R. D. Britt, W. H. Casey, *Chem. - Eur. J.* **2012**, *18*, 10476.

[36] Y. Surendranath, D. A. Lutterman, Y. Liu, D. G. Nocera, *J. Am. Chem. Soc.* **2012**, *134*, 6326.

[37] D. K. Bediako, C. Costentin, E. C. Jones, D. G. Nocera, J.-M. Savéant, *J. Am. Chem. Soc.* **2013**, *135*, 10492.

[38] Y. Liu, D. G. Nocera, *J. Phys. Chem. C* **2014**, *118*, 17060.

[39] M. Risch, F. Ringleb, M. Kohlhoff, P. Bogdanoff, P. Chernev, I. Zaharieva, H. Dau, *Energy Environ. Sci.* **2015**, *8*, 661.

[40] C. Costentin, T. R. Porter, J.-M. Saveant, *J. Am. Chem. Soc.* **2016**, *138*, 5615.

[41] J. G. Mcalpin, Y. Surendranath, M. Dincă, T. A. Stich, S. A. Stoian, W. H. Casey, D. G. Nocera, R. D. Britt, *J. Am. Chem. Soc.* **2010**, *132*, 6882.

[42] C. L. Farrow, D. K. Bediako, Y. Surendranath, D. G. Nocera, S. J. L. Billinge, *J. Am. Chem. Soc.* **2013**, *135*, 6403.

[43] C. Pasquini, I. Zaharieva, D. Gonzalez-Flores, P. Chernev, M. R. Mohammadi, L. Guidoni, R. D. L. Smith, H. Dau, *J. Am. Chem. Soc.* **2019**, *141*, 2938.

[44] M. D. Symes, Y. Surendranath, D. A. Lutterman, D. G. Nocera, *J. Am. Chem. Soc.* **2011**, *133*, 5174.

[45] Y. Surendranath, M. Dinca, D. G. Nocera, *J. Am. Chem. Soc.* **2009**, *131*, 2615.

[46] J. B. Gerken, E. C. Landis, R. J. Hamers, S. S. Stahl, *ChemSusChem* **2010**, *3*, 1176.

[47] T. Naito, T. Shinagawa, T. Nishimoto, K. Takanabe, *ChemSusChem* **2020**, *13*, 5921.

[48] Y. Dong, S. Komarneni, *Small Methods* **2021**, *5*, 2000719.

[49] T. Nishimoto, T. Shinagawa, T. Naito, K. Takanabe, *ChemSusChem* **2021**, *14*, 1554.

[50] D. G. Nocera, *Acc. Chem. Res.* **2012**, *45*, 767.

[51] M. W. Kanan, Y. Surendranath, D. G. Nocera, *Chem. Soc. Rev.* **2009**, *38*, 109.

[52] J. Wang, H. C. Zeng, *ACS Appl. Mater. Interfaces* **2018**, *10*, 6288.

[53] M. Yoshida, T. Mineo, Y. Mitsutomi, F. Yamamoto, H. Kurosu, S. Takakusagi, K. Asakura, H. Kondoh, *Chem. Lett.* **2015**, *45*, 277.

[54] H. Kim, J. Park, I. Park, K. Jin, S. E. Jerng, S. H. Kim, K. T. Nam, K. Kang, *Nat. Commun.* **2015**, *6*, 8253.

[55] H. Dau, C. Pasquini, *Inorganics* **2019**, *7*, 20.

[56] T. Shinagawa, M. T.-K. Ng, K. Takanabe, *ChemSusChem* **2017**, *10*, 4155.

[57] J. He, Y. Peng, Z. Sun, W. Cheng, Q. Liu, Y. Feng, Y. Jiang, F. Hu, Z. Pan, Q. Bian, S. Wei, *Electrochim. Acta* **2014**, *119*, 64.

[58] C. Costentin, D. G. Nocera, *J. Phys. Chem. C* **2019**, *123*, 1966.

[59] C. Pasquini, S. Liu, P. Chernev, D. Gonzalez-Flores, M. R. Mohammadi, P. Kubella, S. Jiang, S. Loos, K. Klingan, V. Sikolenko, S. Mebs, M. Haumann, S. Beyer, L. D'Amario, R. D. L. Smith, I. Zaharieva, H. Dau, *Anal. Bioanal. Chem.* **2021**, *413*, 5395.

[60] H. Dau, P. Liebisch, M. Haumann, *Anal. Bioanal. Chem.* **2003**, *376*, 562.

[61] X. Bo, R. K. Hocking, S. Zhou, Y. Li, X. Chen, J. Zhuang, Y. Du, C. Zhao, *Energy Environ. Sci.* **2020**, *13*, 4225.

[62] M. Huynh, D. K. Bediako, D. G. Nocera, *J. Am. Chem. Soc.* **2014**, *136*, 6002.

[63] T. Honda, K. Murase, T. Hirato, Y. Awakura, *J. Appl. Electrochem.* **1998**, *28*, 617.

[64] R. C. Wolfe, K. G. Weil, B. A. Shaw, H. W. Pickering, *J. Electrochem. Soc.* **2005**, *152*, B82.

[65] C. A. Morris, C.-C. Chen, T. Ito, L. A. Baker, *J. Electrochem. Soc.* **2013**, *160*, H430.

[66] K. Yang, R. Kas, W. A. Smith, *J. Am. Chem. Soc.* **2019**, *141*, 15891.

[67] X. Lu, C. Zhu, Z. Wu, J. Xuan, J. S. Francisco, H. Wang, *J. Am. Chem. Soc.* **2020**, *142*, 15438.

[68] D. A. Henckel, M. J. Counihan, H. E. Holmes, X. Chen, U. O. Nwabara, S. Verma, J. Rodríguez-López, P. J. A. Kenis, A. A. Gewirth, *ACS Catal.* **2021**, *11*, 255.

[69] M. C. O. Monteiro, X. Liu, B. J. L. Hagedoorn, D. D. Snabilié, M. T. M. Koper, *ChemElectroChem* **2021**, *9*, 202101223.

[70] K. Klingan, T. Kottakkat, Z. P. Jovanov, S. Jiang, C. Pasquini, F. Scholten, P. Kubella, A. Bergmann, B. Cuenya, C. Roth, H. Dau, *ChemSusChem* **2018**, *11*, 3449.

[71] C. Pasquini, L. D'Amario, I. Zaharieva, H. Dau, *J. Chem. Phys.* **2020**, *152*, 194202.

[72] K. Obata, R. Van De Krol, M. Schwarze, R. Schomäcker, F. F. Abdi, *Energy Environ. Sci.* **2020**, *13*, 5104.